

Inverse-designed dispersive time-modulated nanostructures

Puneet Garg*, Jan David Fischbach, Aristeidis G. Lampryanidis, Xuchen Wang,
Mohammad S. Mirmoosa, Viktor S. Asadchy, Carsten Rockstuhl*, and Thomas J. Sturges*

P. Garg, Dr. A. G. Lampryanidis, Prof. C. Rockstuhl
Institute of Theoretical Solid State Physics, Karlsruhe Institute of Technology, Kaiserstr. 12,
76131 Karlsruhe, Germany

Email Address: puneet.garg@kit.edu; carsten.rockstuhl@kit.edu

J. D. Fischbach, Prof. C. Rockstuhl, Dr. T. J. Sturges

Institute of Nanotechnology, Karlsruhe Institute of Technology, Kaiserstr. 12, 76131 Karlsruhe,
Germany

Email Address: thomas.sturges@kit.edu

Dr. X. Wang

Qingdao Innovation and Development Base, Harbin Engineering University, Qingdao 266400,
China

Dr. M. S. Mirmoosa

Department of Physics and Mathematics, University of Eastern Finland, Joensuu, Finland

Prof. V. S. Asadchy

Department of Electronics and Nanoengineering, Aalto University, Espoo, Finland

Keywords: *Time-modulated media, photonic inverse design, decay rate enhancement, asymmetric transmission*

Time-modulated nanostructures allow us to control the spatial and temporal properties of light. The temporal modulation of the nanostructures constitutes an additional degree of freedom to control their scattering properties on demand and in a reconfigurable manner. However, these additional parameters create a vast design space, raising challenges in identifying optimal designs. Therefore, tools from the field of photonic inverse design must be used to optimize the degrees of freedom of the system to facilitate predefined optical responses. To further develop this field, here we introduce a differentiable transition (T-) matrix-based inverse design framework for dispersive time-modulated nanostructures. The electron density of the material of the nanostructures is modulated non-adiabatically as a generic periodic function of time. Using the inverse design framework, the temporal shape of the electron density can be manipulated to reach the target functionality. Our computational framework is exploited, exemplarily, in two instances. First, the decay rate enhancement of oscillating dipoles near time-modulated spheres is controlled on demand. Second, using spatiotemporal metasurfaces, a system supporting asymmetric transmission of light at visible frequencies is designed. Our work paves the way toward programmable spatiotemporal metasurfaces and space-time crystals for a future generation of reconfigurable functional photonic devices.

1 Introduction

Time-modulated nanostructures facilitate the simultaneous manipulation of light's spatial and temporal properties [1]. In this context, time modulation refers to changing the material properties as a function of time [2–4]. Additionally, in the case of nanostructures, we consider spatially localized structured objects. Recently, various applications exploiting time-modulated media have been reported. Some of them are made from spatially homogeneous, and some of them are made from spatially structured materials. These applications include parametric amplification [5, 6], nonreciprocal light propagation [7, 8], asymmetric frequency conversion [9], power combining of waves [10], temporal aiming [11], inverse prisms [12], wave freezing [13], anti-reflection temporal coatings [14, 15], perfect absorption [16, 17], polarization conversion [9, 18, 19], spatiotemporal wavefront shaping [20], and so forth. Besides, various experimental advancements in the field of time-modulated materials have fueled the interest of the photonics community in this research domain [21–27]. Owing to the tunability of the temporal modulation, several reconfigurable devices

with desired functionalities can be realized using such dynamic materials [26, 28, 29]. It has to be emphasized that the ability to drastically change the optical response of photonic structures after fabrication is in striking contrast to most conventional systems whose properties are fixed upon fabrication. Of course, multiple other approaches exist to tune the optical response after fabrication, but a temporal modulation seems to be particularly versatile.

Generally, the temporal modulation unlocks additional degrees of freedom to control the flow of light. However, these additional parameters are a blessing and a curse in that they create a vast design space but simultaneously challenge the identification of optimal designs. It prompts the use of tools from the field of photonic inverse design, a framework well established by now to design optical devices with tailored functionality [30–33]. Generally, photonic inverse design is used to iteratively optimize the parameters of a nanostructure toward a design that fulfills a predefined optical functionality [30]. It frequently utilizes fully differentiable software tools that incorporate built-in adjoint solvers, allowing for the optimization of devices with numerous design parameters through a gradient-based method.

Photonic inverse design has already been used to engineer the interaction of light with time-modulated systems. Examples include optical pulse shaping for their enhanced interaction with temporally periodic media [34], unidirectional scattering from disordered photonic time crystals [35], topological state design for photonic time crystals [36], non-reciprocal light propagation from spatiotemporal nanostructures [37], and spectral control of light from time-modulated dispersionless spheres [38]. It is important to remark that most materials, whose properties can be modulated as a function of time with modulation frequencies comparable to the oscillation frequency of light (i.e., non-adiabatic modulation), exhibit dispersion in the optical regime [39–41]. However, to the best of the authors’ knowledge, a study involving the photonic inverse design of dispersive and non-adiabatically modulated optical nanostructures has not yet been reported.

To effectively use the techniques from the field of photonic inverse design, the forward problem needs to be solved efficiently at first. Using traditional full-wave Maxwell solvers to model such nanostructures, e.g., based on the finite-element method, is often computationally expensive [42, 43]. However, a particularly useful formalism to model such nanostructures efficiently is the transition matrix (also known as the T-matrix) formalism [44]. The T-matrix encapsulates the linear scattering response of the considered nanostructure. Once the T-matrix is known, we can calculate the field scattered off the nanostructure for an arbitrary illumination. In fact, given the T-matrix of a finite scatterer, one can compute the effective T-matrix of an infinite periodic arrangement of such a scatterer using the Ewald summation technique [45, 46]. That approach allows us to study the optical response from spatiotemporal metasurfaces. Furthermore, the T-matrix model can be made differentiable, enabling gradient-based optimization techniques to be applied to designing the underlying nanostructures.

In this article, we propose a differentiable T-matrix-based inverse design framework that incorporates material dispersion and non-adiabatic temporal modulations. Our framework can handle time-modulated spheres and spatiotemporal metasurfaces made from such spheres. We assume the underlying material of the spheres to have a generic time-periodic electron density. We model these time-modulated nanostructures using the differentiable T-matrix formalism. Moreover, we use a gradient-based optimization technique to tailor the scattering characteristics of the nanostructures on demand. In particular, we optimize the temporal profile of the electron density of the underlying material to reach the desired optical responses for the nanostructures. Utilizing the proposed inverse design framework, we showcase its applicability in two key examples. First, we design the electron density of the material of a sphere such that a dipole near it exhibits anomalous Drexhage effect. Second, we design the electron density of the material of a spatiotemporal

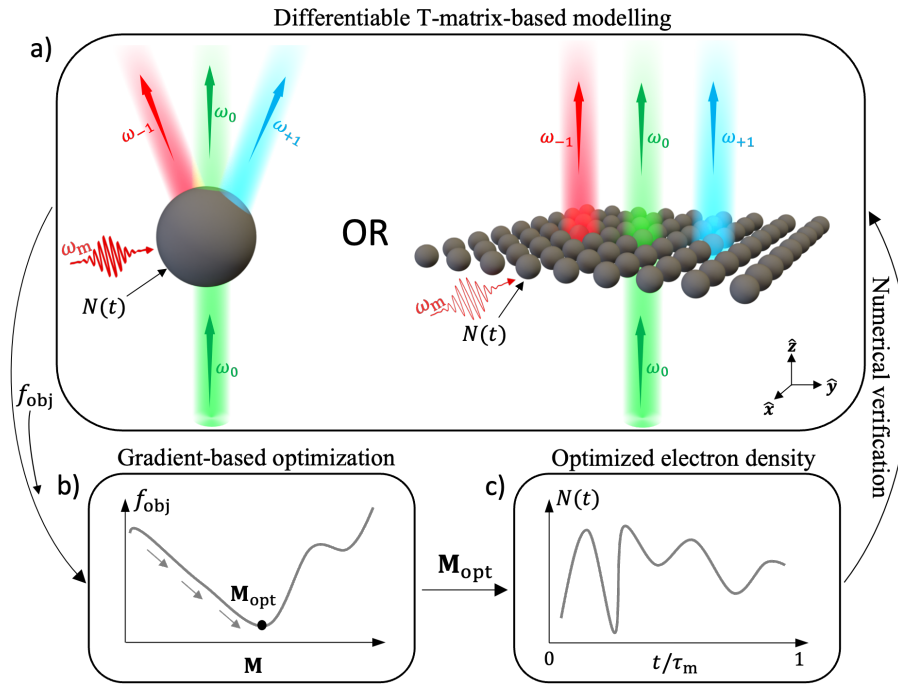


Figure 1: Inverse design framework. First, a time-modulated sphere or spatiotemporal metasurface, as shown in (a), is numerically set up using the differentiable T-matrix-based model. Then, depending on the desired functionality of the considered nanostructure, an objective function $f_{\text{obj}}(\mathbf{M})$ is defined. The time variance of the nanostructure is encoded in the Fourier coefficients \mathbf{M} of the electron density $N(t)$. Next, f_{obj} is minimized or maximized using gradient-based optimization as shown in (b). The optimization returns the optimal Fourier coefficients $\mathbf{M} = \mathbf{M}_{\text{opt}}$ that correspond to an optimal time-varying electron density $N(t)$ shown in (c). Finally, the optimization results are numerically verified for the desired functionality by a forward simulation of the considered nanostructure having the optimal $N(t)$. Here, $\tau_m = 2\pi/\omega_m$ corresponds to the period of the temporal modulation.

metasurface that leads to an efficient frequency upconversion in transmission. This metasurface is then cascaded with a narrow-band frequency filter to realize the asymmetric transmission of light. Importantly, the parameters of the system are chosen so that asymmetric transmission is achieved for visible light.

2 Inverse design framework

In this section, the inverse design framework used to optimize the time-modulated nanostructures is presented (see **Figure 1**). We begin by outlining the differentiable T-matrix method used for modeling time-modulated nanostructures. Then, we describe the gradient-based optimization procedure.

2.1 Differentiable T-matrix method

In this article, we optimize the optical properties of time-modulated spheres and spatiotemporal metasurfaces (see Figure 1(a)). The considered spatiotemporal metasurfaces are periodic arrays of time-modulated spheres arranged in two dimensions (2D). We assume these nanostructures to be made from a dispersive material whose electron density $N(t)$ is a periodic function of time, with a period of $\tau_m = 2\pi/\omega_m$. Here, we consider the non-adiabatic modulation regime, where ω_m is comparable to the oscillation frequency of light. Such a time-varying electron density $N(t)$ is incorporated into our analysis using the Drude dispersion model [42, 43] (see Supporting Infor-

mation; Section S1). Note that for all the examples in this manuscript, we use Drude parameters that resemble the properties of gold at frequencies below its plasma frequency [47]. Such a choice is made as gold exhibits strong dispersion at visible frequencies that are of interest in this work. Importantly, due to the time modulation of the nanostructures, an incident excitation with frequency ω gives rise to a polychromatic scattered field with frequencies $\omega_j = \omega + j\omega_m$, with $j \in \mathbb{Z}$ (see Figure 1(a)).

As mentioned earlier, linear optical nanostructures can be numerically modeled using the T-matrix method [44]. The T-matrix is an efficient tool to semi-analytically model optical nanostructures based on Mie theory [48]. It can handle finite scatterers and photonic materials made from an infinite periodic arrangement of such scatterers. The T-matrix formalism involves expanding the incident field \mathbf{E}^{inc} and scattered field \mathbf{E}^{sca} for the nanostructure in a basis of vector spherical harmonics (see the Methods section). Let \mathbf{A}^{inc} and \mathbf{A}^{sca} be the corresponding incident and scattered coefficient vectors, respectively. Then, \mathbf{A}^{inc} and \mathbf{A}^{sca} satisfy

$$\mathbf{A}^{\text{sca}} = \hat{\mathbf{T}} \cdot \mathbf{A}^{\text{inc}}, \quad (1)$$

where $\hat{\mathbf{T}}$ is the so-called T-matrix of the considered nanostructure. From Equation (1), we note that the T-matrix completely encapsulates the scattering response of the nanostructure. Once the T-matrix of the nanostructure is known, the field scattered off it can be calculated easily using Equation (1). The T-matrix for static scatterers can be computed analytically or using full-wave Maxwell solvers [49–51]. Recently, the T-matrix formalism has also been applied to time-modulated nanostructures [38, 42, 43, 52–54]. The T-matrices of dispersive time-modulated spheres and spatiotemporal metasurfaces made from these time-modulated spheres are analytically known [42, 43]. We use these existing T-matrices for our purposes. We wish to highlight here that Equation (1) also holds for the time-modulated nanostructures. In that case, the size of $\hat{\mathbf{T}}$ depends on the number of scattered frequencies ω_j and considered vector spherical harmonics (see the Methods section). Furthermore, it is important to mention that we wrote our T-matrix-based code using JAX, a software package that can automatically differentiate native Python and Numpy functions [55]. Therefore, it makes our T-matrix model differentiable, allowing us to use a gradient-based optimization as discussed in the following.

2.2 Optimization procedure

Having established the differentiable T-matrix-based model, we next discuss the optimization procedure. We use a gradient-based optimization approach. We begin by expanding $N(t)$ in a Fourier series as

$$N(t) = N_0 \left[1 + \sum_{q=1}^Q (M_q e^{-iq\omega_m t} + \text{c.c.}) \right]. \quad (2)$$

Here, N_0 corresponds to the electron density of the static material, the different M_q correspond to the complex Fourier coefficients of $N(t)$, Q is the total number of considered M_q coefficients, and c.c. refers to the complex conjugate. The electron density $N(t)$ is non-negative and real-valued. We define a vector \mathbf{M} that contains all the coefficients M_q for brevity. Then, depending on the desired functionality of the time-modulated nanostructure, an objective function $f_{\text{obj}}(\mathbf{M})$ is defined. The objective function f_{obj} takes \mathbf{M} as the design variables. Note that the base modulation frequency ω_m is chosen *a priori* and does not enter the optimization procedure.

Next, depending on the design goal, f_{obj} is either minimized or maximized using gradient-based optimization (see Figure 1(b)). As mentioned earlier, the differentiable T-matrix-based model

allows us to compute the derivatives of f_{obj} with respect to \mathbf{M} . Additionally, thanks to the reverse-mode automatic differentiation, we obtain the derivatives of f_{obj} with respect to all $M_q \in \mathbf{M}$ with a single backward pass through the simulation [56]. More details on the software packages can be found in Supporting Information; Subsection S2.1. Using the gradient information, we iteratively update \mathbf{M} until a local minimum/maximum of f_{obj} is reached (see Figure 1(b)). Such an optimization returns the optimal Fourier coefficient vector $\mathbf{M} = \mathbf{M}_{\text{opt}}$, and correspondingly, the optimal time-modulated electron density $N(t)$ (see Figure 1(c)). Finally, we numerically verify if the desired functionality is reached by running a forward simulation with the optimal $N(t)$ (see Figure 1(a)). Note that the details of various convergence parameters used for calculations in this manuscript are available in the Supporting Information.

Having introduced the inverse design framework, we now exploit it to study two distinct phenomena. First, we tailor the electron density of the material of a time-modulated sphere so that a dipole in its vicinity displays anomalous Drexhage effect. Next, we present an example based on the spatiotemporal metasurfaces to realize asymmetric transmission of light at visible frequencies.

3 Radiative decay rate enhancement

Nanostructures are extensively used in the photonics community to enhance the spontaneous radiative decay rates of excited atoms [57–59]. In classical theory, an excited atom can be modeled as an oscillating point electric dipole [60]. Recently, there has been a growing interest in studying the spontaneous decay rates of dipoles in the vicinity of time-modulated media [61–64]. Time-modulated media are non-Hermitian systems, as they can supply (leading to optical gain) and absorb (leading to optical loss) energy to and from the incident electromagnetic fields. However, optical gain necessitates a careful examination of the existing approaches to calculate the decay rates of dipoles near such non-Hermitian systems [65, 66]. Therefore, for the dipoles in the vicinity of time-modulated nanostructures, the effects of optical gain on their spontaneous decay rate calculation must be considered. The optical gain can be interpreted as a spontaneous excitation of the atom from its ground to an excited state, eventually leading to the subsequent emission of a photon [63, 65]. Here, the excitation of the atom is not photon-mediated; rather it occurs due to the non-adiabatic quantum pumping induced by the time-periodic material [63, 65]. Note that non-adiabatic quantum pumping is a process where a system, due to rapid time modulation, cannot respond instantaneously and consequently ceases to remain in its ground state [67]. The calculation of the decay rates of dipoles in the vicinity of time-periodic media has been shown in various works [61–64]. However, a computation of the decay rates of dipoles kept near spatially finite time-modulated media has not yet been presented. Finite media are advantageous as they allow greater flexibility in positioning the dipoles near them. In the following, using the arguments of [66], we derive an expression for the radiative decay rate enhancement of a dipole kept near a time-modulated sphere while considering the optical gain (and loss) from the sphere.

3.1 Derivation of the radiative decay rate enhancement

The power conservation relation for a dipole kept in the vicinity of an arbitrary active (gain providing) and an arbitrary absorbing resonator reads as [66, Equation (21)]

$$P_{\text{far}} = P_{\text{LDOS}} + P_{\text{gain}} - P_{\text{abs}}. \quad (3)$$

Here, P_{far} refers to the total power radiated by the system formed by the dipole and the resonators in the far field, P_{LDOS} refers to the net power crossing an imaginary surface enclosing only the dipole, P_{gain} refers to the total power gained by the system due to the active resonator, and P_{abs}

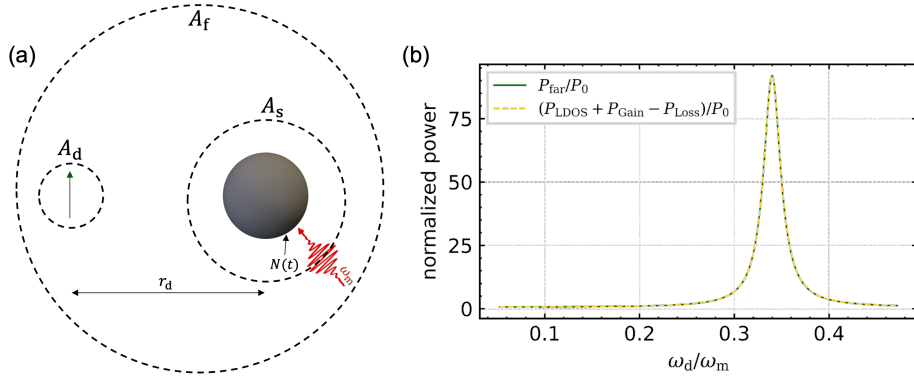


Figure 2: (a) A system consisting of an electric dipole near a time-modulated sphere. (b) Normalized powers plotted as a function of the emission frequency ω_d of the dipole for the system shown in (a). Here, the time-varying electron density of the sphere is given by $N(t) = N_0[1 + 0.8\cos(\omega_m t)]$, and its radius is $R = 10$ nm. Furthermore, the dipole is kept at a distance $r_d = 15$ nm from the center of the sphere. Moreover, $\omega_m = 0.17c_0/R$ with c_0 being the speed of light in vacuum.

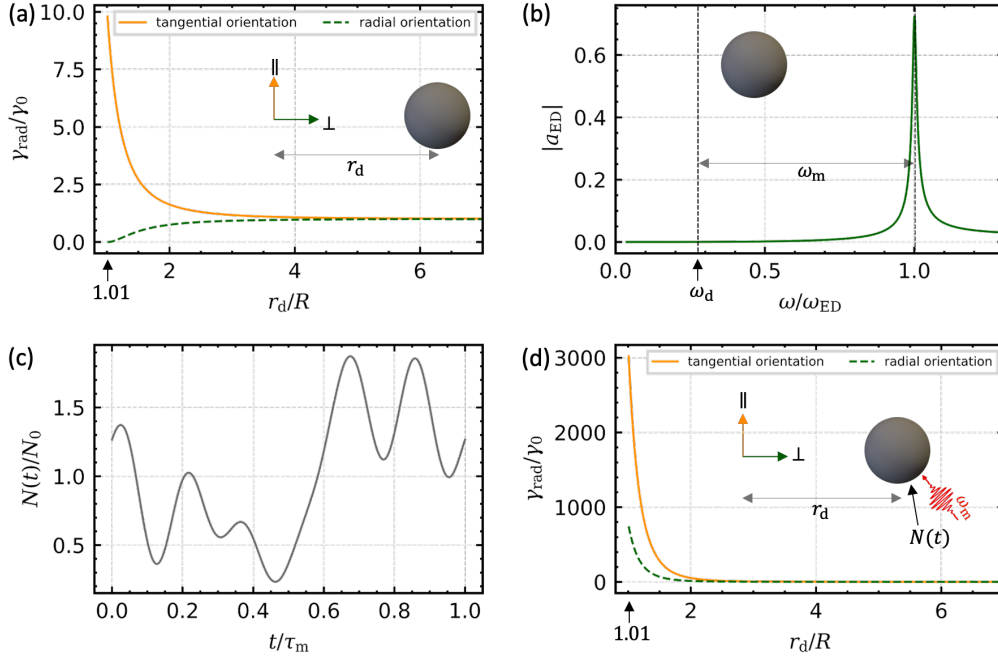


Figure 3: Anomalous Drexhage Effect. (a) The radiative decay rate enhancement $\gamma_{\text{rad}}/\gamma_0$ for an electric dipole as a function of its distance r_d from the center of a static sphere for its two orthogonal polarizations. (b) The absolute value of the electric dipolar Mie coefficient of the static sphere as a function of the excitation frequency ω . (c) The optimized electron density $N(t)$ that maximizes $\gamma_{\text{rad}}/\gamma_0$ for the radially orientated dipole (\perp -polarization) at $r_d/R = 1.01$. (d) The radiative decay rate enhancement $\gamma_{\text{rad}}/\gamma_0$ of the dipole in two orthogonal polarizations as a function of its distance r_d from the time-modulated sphere having the optimized $N(t)$ shown in (c).

refers to the total power absorbed by the lossy resonator from the system. Note that, in our analysis, time-averaged powers are considered.

We aim to derive an expression for the radiative decay rate enhancement of a dipole kept near a time-modulated sphere (see **Figure 2(a)**). As mentioned earlier, a time-modulated sphere acts as a medium that can supply and absorb energy to and from the fields incident on it. As Equation (3) holds for dipoles near arbitrary gain-loss resonators, it must also hold for a system consisting of a dipole kept near a time-modulated sphere. However, Equation (3) was initially written for dipoles near static gain media [66]. Therefore, it must be first verified for the system involving time-modulated media. To test Equation (3), we plot the values of the left and right-hand sides independently as a function of the emission frequency ω_d of the dipole in Figure 2(b). In the context of such a sphere-dipole system, P_{far} , P_{LDOS} , and $P_{\text{gain}} - P_{\text{loss}}$ refer to the net powers crossing the surfaces A_f , A_d , and A_s , respectively (see Figure 2(a)). Here, A_f , A_d , and A_s correspond to the surfaces enclosing both the sphere and dipole, only the dipole, and only the sphere, respectively. Note that we use the T-matrix method to calculate these powers (see Supporting Information; Section S3). Furthermore, in Figure 2(b), the plotted powers are normalized by the power P_0 radiated by the dipole in a vacuum. From Figure 2(b), we observe that the power conservation relation given in Equation (3) also holds for the sphere-dipole system. Next, the gain corrected expression for the total emitted power by the dipole $P_{\text{total}}^{\text{dip}}$ that is responsible for its spontaneous decay in the presence of such a non-Hermitian sphere is [66, Equation (23)]

$$P_{\text{total}}^{\text{dip}} = P_{\text{LDOS}} + P_{\text{gain}}. \quad (4)$$

Moreover, using Equation (3) and (4), we can write $P_{\text{far}} = P_{\text{total}}^{\text{dip}} - P_{\text{abs}}$. Note that $P_{\text{total}}^{\text{dip}} - P_{\text{abs}}$ corresponds to the net radiatively emitted power from the dipole $P_{\text{rad}}^{\text{dip}}$ that leads to its spontaneous *radiative* decay [68, 69]. Therefore, we conclude that $P_{\text{far}} = P_{\text{rad}}^{\text{dip}}$. Finally, the radiative decay rate enhancement $\gamma_{\text{rad}}/\gamma_0$ of the dipole kept near a time-modulated sphere can be written as

$$\frac{\gamma_{\text{rad}}}{\gamma_0} = \frac{P_{\text{rad}}^{\text{dip}}}{P_0} = \frac{P_{\text{far}}}{P_0}. \quad (5)$$

Here, γ_{rad} refers to the radiative decay rate of the dipole in the presence of the time-modulated sphere, and γ_0 refers to the decay rate of the dipole in a vacuum.

Having discussed the details of decay rate calculation, we proceed to apply our inverse design framework to engineer the radiative decay rate enhancement of the dipoles near time-modulated spheres on demand.

3.2 Anomalous Drexhage Effect

In 1970, K.H. Drexhage showed that the radiative decay rate enhancement of a dipole kept near a perfect mirror depends on the orientation of the dipole to the surface of the mirror [70]. A similar effect is observed for a dipole near a *static* sphere, as shown in **Figure 3(a)**. Here, we plot the radiative decay rate enhancement $\gamma_{\text{rad}}/\gamma_0$ of an electric dipole for its two orthogonal polarizations as a function of the distance r_d from the center of a static sphere. Note that \perp -polarization refers to the radial and \parallel -polarization refers to the tangential orientation of the dipole with respect to the sphere. The radius of the sphere is $R = 10$ nm, and the emission frequency of the dipole is $\omega_d = 0.072c_0/R$. Here, c_0 is the speed of light in vacuum.

From Figure 3(a), we observe that the decay rate enhancement shows different trends as a function of the distance r_d for the two orientations of the dipole. Consider the regime $r_d/R \approx 1$. For the

radial orientation, the decay rate is almost negligible leading to $\gamma_{\text{rad}}/\gamma_0 \approx 0$. In contrast, the decay rate is significant for the tangential orientation leading to $\gamma_{\text{rad}}/\gamma_0 \gg 1$. Such an orientation-dependent decay rate enhancement of the dipole is known as the Drexhage effect [70].

The physical explanation for the Drexhage effect is as follows. To begin with, the decay rate enhancement of the dipole depends on the total far field [68, 71] (see Equation (5)). The total far field $\mathbf{E}^{\text{tot}}(\mathbf{r}_{\text{far}})$ is the sum of the field scattered from the sphere $\mathbf{E}^{\text{sca}}(\mathbf{r}_{\text{far}})$ and the field of the dipole itself $\mathbf{E}^{\text{dip}}(\mathbf{r}_{\text{far}})$, in the absence of the sphere, at a spatial location $\mathbf{r} = \mathbf{r}_{\text{far}}$. Here, $r_{\text{far}} \gg R$. For the example shown in Figure 3(a), \mathbf{E}^{sca} and \mathbf{E}^{dip} interfere destructively (constructively) for the radial (tangential) orientation of the dipole leading to negligible (significant) decay rate enhancement. Besides, for $r_{\text{d}}/R \gg 1$, for both the orientations of the dipole, $\gamma_{\text{rad}}/\gamma_0$ saturates to unity. This saturation happens because \mathbf{E}^{sca} decays rapidly as r_{d} increases, leading to a decrease in the interference effects of the fields and consequently the impact of the sphere on γ_{rad} [68]. Therefore, γ_{rad} approaches γ_0 for $r_{\text{d}}/R \gg 1$.

Having discussed the Drexhage effect, we explore the anomalous Drexhage effect next. It refers to a situation where a dipole shows a similar decay rate enhancement for its two orthogonal orientations. This is considered here as anomalous because it is in striking contrast to the Drexhage effect that has been studied from multiple perspectives [72, 73]. Our goal is to show such an anomalous Drexhage effect by an appropriate time modulation of the sphere. To do so, we design the time-varying electron density $N(t)$ of the sphere such that, even for the radial orientation of the dipole, we have a significant decay rate enhancement for $r_{\text{d}}/R \approx 1$. Therefore, we maximize $\gamma_{\text{rad}}/\gamma_0$ for $r_{\text{d}}/R \approx 1$ for the radial orientation of the dipole. From Equation (5), we observe that $\gamma_{\text{rad}}/\gamma_0$ is proportional to the power emitted in the far field by the sphere-dipole system P_{far} . Consequently, our task at hand is reduced to maximizing P_{far} when the dipole is placed sufficiently close to the sphere. We choose $r_{\text{d}} = 1.01R$.

To set up the optimization problem, we define our objective function f_{obj} in terms of P_{far} (see the Methods section). Note that besides P_{far} , f_{obj} also consists of a penalty function that penalizes the optimizer if $N(t)$ tends toward negative values for any $t \in [0, \tau_{\text{m}}]$. We use such a penalty function with all other objective functions in this article. Additionally, we need to fix the base modulation frequency ω_{m} *a priori* in the optimization. To choose ω_{m} such that it assists the maximization of P_{far} , we first plot the amplitude of the electric dipolar Mie coefficient a_{ED} of the static sphere as a function of the excitation frequency ω [74] (see Figure 3(b)). From Figure 3(b), we observe the existence of the electric dipolar resonance of the sphere at $\omega = \omega_{\text{ED}}$. Therefore, we choose $\omega_{\text{m}} = \omega_{\text{ED}} - \omega_{\text{d}}$. Such a choice is made because once the time modulation is turned on, the sphere in the presence of the dipole emitting at the frequency ω_{d} scatters the frequencies $\omega_j = \omega_{\text{d}} + j\omega_{\text{m}}$, with $j \in \mathbb{Z}$ (see Figure 1(a)). Therefore, $\omega_1 = \omega_{\text{ED}}$ lies exactly at the electric dipolar resonance frequency leading to a resonant enhancement of P_{far} in the time-modulated case for an appropriately optimized $N(t)$ (see Equation (S3) of Supporting Information).

Having chosen f_{obj} and ω_{m} , we use the inverse design framework discussed in Section 2 to maximize $\gamma_{\text{rad}}/\gamma_0$ for the dipole oriented radially to the time-modulated sphere at $r_{\text{d}} = 1.01R$. The optimized $N(t)$ is shown in Figure 3(c). Furthermore, in Figure 3(d), we plot $\gamma_{\text{rad}}/\gamma_0$ as a function of r_{d} for the dipole near the time-modulated sphere. From Figure 3(d), we observe that for both the radial and tangential orientations of the dipole, the decay rate enhancement is significant (i.e., $\gamma_{\text{rad}}/\gamma_0 \gg 1$) for $r_{\text{d}}/R \approx 1$, leading to a demonstration of the anomalous Drexhage effect.

In particular, as intended, the optimization successfully returns an $N(t)$ that maximizes $\gamma_{\text{rad}}/\gamma_0$ when $r_{\text{d}}/R \approx 1$ for the radial orientation of the dipole. Such a maximization can be explained as follows. As expected, the temporal modulation with the optimized $N(t)$ enhances the total far

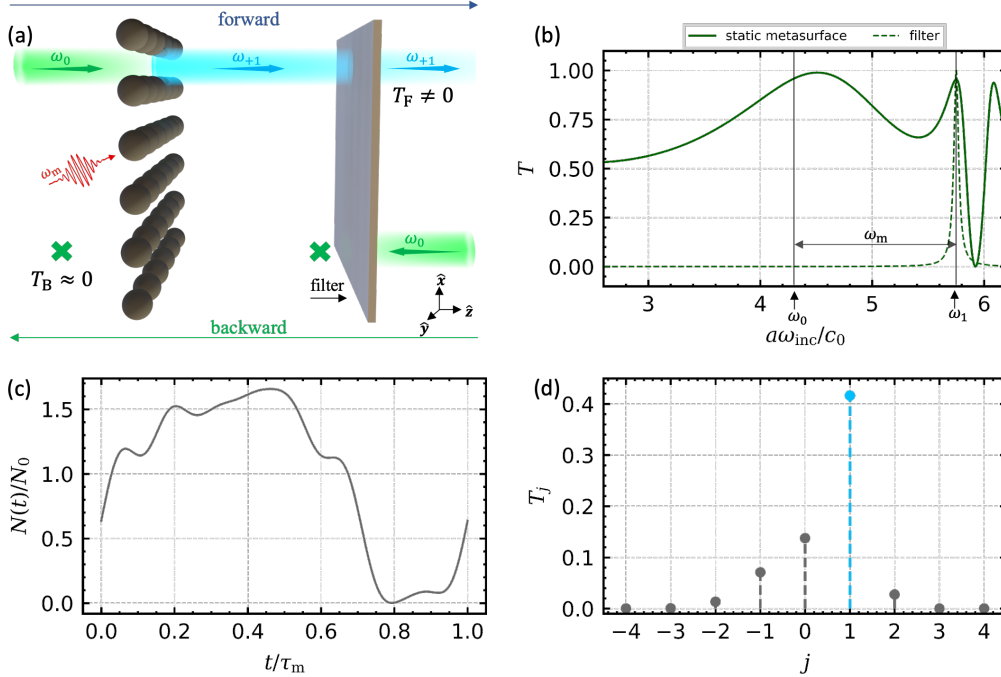


Figure 4: Asymmetric transmission (AT) of light at visible frequencies. (a) A conceptual illustration of an AT system formed by cascading a spatiotemporal metasurface and a narrow-band filter. Here, T_F (T_B) corresponds to the final forward (backward) transmissivity of the AT system. (b) The transmissivity T of the metasurface under static operation (solid curve) and filter (dotted curve) as shown in (a) as a function of the incident frequency ω_{inc} . (c), (d) The optimized electron density $N(t)$ as a function of time t , and the corresponding transmissivity contribution T_j of the spatiotemporal metasurface as a function of the harmonic number j , respectively.

field $\mathbf{E}^{\text{tot}}(\mathbf{r}_{\text{far}})$ at $\omega_j = \omega_1$ (see Supplementary Information; Section S4). Moreover, since the power P_{far} depends on the contributions of $\mathbf{E}^{\text{tot}}(\mathbf{r}_{\text{far}})$ across all the frequencies ω_j , this field enhancement at ω_1 maximizes P_{far} , which in turn maximizes the decay rate enhancement. Additionally, even for the tangential orientation of the dipole, $\gamma_{\text{rad}}/\gamma_0$ at $r_d/R \approx 1$ is about 300 times higher in the time-modulated case than that in the static case. Such a high $\gamma_{\text{rad}}/\gamma_0$ for the tangential orientation also occurs due to a similar total far field enhancement.

As discussed in the following, we now apply our inverse design framework to a system involving spatiotemporal metasurfaces.

4 Asymmetric transmission of light at visible frequencies

As the second application of our inverse design framework, we design a device that implements asymmetric transmission (AT) of light at visible frequencies. A device operating under the AT condition allows efficient transmission of light in one direction while blocking it in the opposite direction [75]. A conceptual illustration of spatiotemporal metasurface-based AT is shown in **Figure 4(a)**. The system shown in Figure 4(a) is formed by cascading a spatiotemporal metasurface and a narrow-band frequency filter.

When an electromagnetic wave at frequency ω_0 is incident to the system from the left-hand side (forward propagation), it encounters the spatiotemporal metasurface that upconverts most of its energy to an electromagnetic wave at frequency $\omega_1 = \omega_0 + \omega_m$. Our design objective is to render this upconversion efficient. The wave then encounters the filter that offers complete transmission to

fields with frequency ω_1 while blocking all other frequencies [76]. Therefore, the wave at frequency ω_1 gets completely transmitted through the filter, leading to a non-zero final forward transmissivity T_F . On the other hand, if a wave at frequency ω_0 is incident from the right-hand side to the system (backward propagation), it encounters the filter first, which does not allow any further propagation of the wave. Therefore, the final backward transmissivity T_B of the whole system is negligible. Note that this AT should not be confused with nonreciprocity [77]. To test the nonreciprocity of our system, the final forward transmitted field at ω_1 must be backpropagated through the system. This backpropagated field must then be compared with the initial incident field at ω_0 . The contrast between the backpropagated field and the time-reversed incident field quantifies the nonreciprocity of the system. Moreover, it is important to mention that the problem of frequency upconversion using spatiotemporal structures was also studied in various other works [26, 78–83]. However, all these works were limited to the adiabatic regime of temporal modulation (i.e., $\omega_m \ll \omega_0$), which requires the use of frequency filters with very narrow bandwidths. Furthermore, the frequency of operation in these works was either in the microwave or infrared regime. In our framework, we use non-adiabatic temporal modulation, our metasurface operates at visible frequencies, and we fully take into account the effects of material dispersion that cannot be ignored for most of the materials at such frequencies.

We aim to design an AT system as shown in Figure 4(a). A critical component of the AT system is the spatiotemporal metasurface, which is capable of frequency upconversion. In what follows, we discuss the choice of parameters of the system deemed to be supportive in achieving an efficient frequency upconversion using the Mie resonances of the underlying static metasurface [54, 84]. To begin with, we assume the metasurface to be made from a square lattice of spheres. The radius R of the spheres is $R = 150$ nm, and the lattice constant a of the metasurface is $a = 2.6R$. Besides, for simplicity, the parameters are chosen such that the metasurface is subwavelength in the spectral range of interest. For a subwavelength metasurface, only the principle spatial diffraction order is propagating. The transmissivity T of the metasurface as a function of the incident frequency ω_{inc} under static conditions (i.e., $N(t) = N_0$) is shown in Figure 4(b). Note that here, and for the following simulations, we assume a monochromatic x -polarized plane wave normally incident on the metasurface for calculating T . From Figure 4(b), we observe that the static metasurface supports various Mie resonances [84].

Using the transmission spectrum of the static metasurface, we choose the frequencies ω_0 and ω_m for the time-modulated operation (see Figure 4(b)). From Figure 4(b), it is apparent that ω_0 and ω_m are chosen such that ω_1 lies at a high-quality resonance of the static metasurface. Such a choice is made so that upon temporal modulation of the metasurface with an appropriately chosen $N(t)$, a resonant enhancement of the transmitted field occurs at ω_1 for an incident field at ω_0 . Importantly, to design the AT functionality of the spatiotemporal metasurface for visible frequencies, the parameters a , R , and ω_m are chosen such that ω_0 and ω_1 lie in the visible spectrum. In our example, $\omega_0 = 2\pi \times 542$ THz and $\omega_1 = 2\pi \times 704$ THz.

Next, we use our inverse design framework to optimize the time-varying electron density $N(t)$ of the spatiotemporal metasurface. The total transmissivity T of the spatiotemporal metasurface can be written as a sum of the contribution of all the transmitted frequency harmonics, i.e., $T = \sum_j T_j$ [43] (see Figure 1(a)). Our goal is to maximize the transmissivity at ω_1 . Therefore, we choose the objective function f_{obj} in terms of T_1 (see the Methods section).

The electron density $N(t)$ as a result of the optimization is shown in Figure 4(c). Furthermore, the corresponding transmissivity contributions T_j as a function of the scattered harmonic number j are shown in Figure 4(d). From Figure 4(d), we observe that the metasurface with the optimal $N(t)$ preferentially transmits the energy of the incident wave to the frequency ω_1 (with $T_1 = 0.42$).

Such a preferential transmission can be explained as follows. To begin with, the time-varying electron density $N(t)$ effectively modulates the amplitude and phase of the time-domain complex transmission coefficient of the metasurface [78] (see Supporting Information; Section S5). In principle, such a modulation of the transmission coefficient gives rise to the transmitted frequencies ω_j (with $j \in \mathbb{Z}$). However, due to the particular choice of f_{obj} , the optimizer converges such that this amplitude and phase modulation leads to an efficient coupling to ω_1 in transmission (also see Supporting Information; Section S6). Additionally, the high-quality resonance of the underlying static metasurface at ω_1 assists in the resonant enhancement of such a coupling (see Figure 4(b)). It is important to remark that such a preferential transmission is insensitive to the phase of the incident wave.

Note that the total transmission efficiency of the optimized spatiotemporal metasurface is about 66%. Approximately 15% of the incident energy is lost to reflection and about 19% to material losses due to frequency dispersion. Moreover, from Figure 4(d), we observe that even though the maximum transmitted energy is linked to ω_1 , a non-zero amount of energy is coupled to other scattered frequencies. To attain a perfect upconversion to the frequency ω_1 (i.e., $T_1 = 1$ and $T_j = 0 \forall j \neq 1$), one needs a spatiotemporal metasurface whose time-domain complex transmission coefficient has a pure linear phase modulation of 2π in the time-period τ_m [78] (see Supporting Information; Section S5). Attaining such an idealized condition is challenging at the optical frequencies [85].

Next, we choose a filter that has almost unity transmissivity T at ω_1 and negligible T at all other frequencies (see the dotted curve in Figure 4(b)). One of the possible implementations of such a filter can be found in [76]. Finally, cascading such a filter with the optimized metasurface results in a final forward transmissivity of $T_F = 0.42$ for a wave incident at $\omega_0 = 2\pi \times 542$ THz. Furthermore, the final backward transmissivity of the system for the same incident wave is $T_B \approx 0$. Therefore, our inverse design framework allows us to realize the asymmetric transmission of light at visible frequencies.

5 Conclusion

We have presented a differentiable T-matrix-based inverse design framework to engineer the scattering response of time-modulated spheres and spatiotemporal metasurfaces on demand. These time-modulated nanostructures are assumed to be made from a dispersive material with a time-varying electron density. Using our inverse design framework, we optimized the temporal profile of the electron density to tailor the desired functionality of the chosen nanostructure. We used a gradient-based approach to perform the optimization. We exploited our inverse design framework in two specific examples.

First, we computed the decay rate enhancement of dipoles kept near time-modulated spheres. In particular, we optimized time-modulated spheres such that the dipoles exhibit anomalous Drexhage effect. Next, we applied our inverse design framework to spatiotemporal metasurfaces. We optimized the metasurface to achieve an efficient frequency upconversion. Such an optimized metasurface is then cascaded with a narrow-band filter so that the composite system supports asymmetric transmission (AT) of light at visible frequencies. This AT operation is achieved while using non-adiabatic temporal modulation and considering the effects of material dispersion.

The T-matrix-based inverse design tool introduced in this article assists in simultaneously controlling the spatial and temporal properties of light. Depending on the choice of the objective function, various applications using the time-modulated nanostructures can be realized in princi-

ple. From this perspective, our approach unlocks the opportunities to design novel photonic time and space-time crystals.

6 Methods

Further details on the differentiable T-matrix method: Let us assume a general polychromatic incident excitation to the considered time-modulated nanostructure with frequencies, $\omega_j = \omega + j\omega_m$ with $j \in [-J, J]$. Here, J is an integer that should be chosen sufficiently large to ensure numerical convergence. Then, the incident field \mathbf{E}^{inc} and scattered field \mathbf{E}^{sca} can be written as

$$\mathbf{E}^{\text{inc}}(\mathbf{r}, t) = \sum_{jl\mu s} A_{jl\mu s}^{\text{inc}} \mathbf{F}_{j\mu s}^{(1)}(k_j \mathbf{r}) e^{-i\omega_j t}, \quad (6a)$$

$$\mathbf{E}^{\text{sca}}(\mathbf{r}, t) = \sum_{jl\mu s} A_{jl\mu s}^{\text{sca}} \mathbf{F}_{l\mu s}^{(3)}(k_j \mathbf{r}) e^{-i\omega_j t}, \quad (6b)$$

where $k_j = \omega_j/c_0$. Besides, $\mathbf{F}_{l\mu s}^{(1)}(x)$ ($\mathbf{F}_{l\mu s}^{(3)}(x)$) represent the regular (radiating) vector spherical harmonics (VSHs) with total angular momentum $l = 1, 2, 3, \dots, l_{\text{max}}$, z -component of angular momentum $\mu = -l, -l+1, \dots, l$, and parity $s = 0, 1$. Here, $s = 0$ represents the transverse-electric (TE), and $s = 1$ represents the transverse-magnetic (TM) mode, respectively. Moreover, l_{max} is the maximum multipolar order retained in the expansion. It should be chosen sufficiently large to ensure numerical convergence. Next, using the method in [42, 43], one can connect \mathbf{A}^{inc} and \mathbf{A}^{sca} by the T-matrix $\hat{\mathbf{T}}$ as given in Equation (1). Note that $\hat{\mathbf{T}}$ is a square matrix with size $2l_{\text{max}}(2J+1)(l_{\text{max}}+2)$.

The objective function for maximizing $\gamma_{\text{rad}}/\gamma_0$: From Equation (3), we observe that γ_{rad} is proportional to P_{far} . Therefore, maximizing γ_{rad} requires the maximization of P_{far} . For the simulation result shown in Figure 3(c) and (d), we found the minimization of the objective function to perform better in terms of convergence. Therefore, we defined the objective function to be minimized as $f_{\text{obj}}(\mathbf{M}) = w/P_{\text{far}}(\mathbf{M}) + (1-w)p(\mathbf{M})$. Here, $p(\mathbf{M})$ is a penalty function that penalizes the optimizer if it goes toward those values of \mathbf{M} that correspond to a negative $N(t)$ for any $t \in [0, \tau_m]$ (see Supporting Information; Subsection 2.2 for more details on $p(\mathbf{M})$). Furthermore, w is a quantity that distributes the weight of the objective function between $1/P_{\text{far}}$ and the penalty p . We chose $w = 0.99$ for this optimization.

The objective function for maximizing T_1 : For the example shown in Figure 4(a), we aim to maximize T_1 . Therefore, we define the objective function to be maximized as $f_{\text{obj}}(\mathbf{M}) = wT_1(\mathbf{M}) - (1-w)p(\mathbf{M})$. Here, as we are maximizing f_{obj} , $p(\mathbf{M})$ has a negative weight. We chose $w = 0.84$ for this optimization.

Supporting Information

Supporting Information is available from the author.

Acknowledgments

The authors would like to thank Dr. Elli Stamatopoulou, and Dr. Markus Nyman for useful discussions about the decay rate enhancement. P.G. and C.R. are part of the Max Planck School of Photonics, supported by the Bundesministerium für Bildung und Forschung, the Max Planck Society, and the Fraunhofer Society. P.G. acknowledges support from the Karlsruhe School of Optics and Photonics (KSOP). P.G. and C.R. acknowledge financial support by the German

Research Foundation within the SFB 1173 (Project-ID No. 258734477). J.D.F. and C.R. acknowledge financial support by the Helmholtz Association in the framework of the innovation platform “Solar TAP”. C.R. acknowledges support from the German Research Foundation within the Excellence Cluster 3D Matter Made to Order (EXC 2082/1 under project number 390761711) and by the Carl Zeiss Foundation. T.J.S. acknowledges funding from the Alexander von Humboldt Foundation. M.S.M. acknowledges support from the Research Council of Finland (Grant No. 336119). V.A. acknowledges the Research Council of Finland (Project No. 356797), Finnish Foundation for Technology Promotion, and Research Council of Finland Flagship Programme, Photonics Research and Innovation (PREIN), decision number 346529, Aalto University. X.W. acknowledges the Fundamental Research Funds for the Central Universities, China (Project No. 3072024WD2603) and the Scientific Research Foundation, Harbin Engineering University, China (Project No. 0165400209002).

References

- [1] N. Engheta, *Science* **2023**, *379*, 6638 1190.
- [2] E. Galiffi, R. Tirole, S. Yin, H. Li, S. Vezzoli, P. Huidobro, M. Silveirinha, R. Sapienza, A. Alù, J. Pendry, *Advanced Photonics* **2022**, *4* 014002.
- [3] G. Ptitsyn, M. S. Mirmoosa, A. Sotoodehfar, S. A. Tretyakov, *IEEE Antennas and Propagation Magazine* **2023**, *65*, 4 10.
- [4] M. M. Asgari, P. Garg, X. Wang, M. S. Mirmoosa, C. Rockstuhl, V. Asadchy, *arXiv preprint arXiv:2404.04899* **2024**.
- [5] J. R. Zurita-Sánchez, P. Halevi, J. C. Cervantes-González, *Phys. Rev. A* **2009**, *79* 053821.
- [6] X. Wang, P. Garg, M. S. Mirmoosa, A. G. Lamprianidis, C. Rockstuhl, V. S. Asadchy, *arXiv preprint arXiv:2310.02786* **2023**.
- [7] A. Shaltout, A. Kildishev, V. Shalaev, *Optical Materials Express* **2015**, *5* 2459.
- [8] P. Huidobro, M. Silveirinha, E. Galiffi, J. Pendry, *Phys. Rev. Appl.* **2021**, *16* 014044.
- [9] M. Mirmoosa, M. Mostafa, A. Norrman, S. Tretyakov, *Physical Review Research* **2024**, *6*, 1 013334.
- [10] X. Wang, V. Asadchy, S. Fan, S. Tretyakov, *ACS Photonics* **2021**, *8* 3034.
- [11] V. Pacheco-Peña, N. Engheta, *Light: Science & Applications* **2020**, *9*, 1 129.
- [12] A. Akbarzadeh, N. Chamanara, C. Caloz, *Optics letters* **2018**, *43*, 14 3297.
- [13] X. Wang, M. S. Mirmoosa, S. A. Tretyakov, *Nanophotonics* **2023**, *12*, 14 2813.
- [14] D. Ramaccia, A. Toscano, F. Bilotti, *Optics Letters* **2020**, *45*, 20 5836.
- [15] V. Pacheco-Peña, N. Engheta, *Optica* **2020**, *7*, 4 323.
- [16] M. Mostafa, A. Díaz-Rubio, M. Mirmoosa, S. Tretyakov, *Physical Review Applied* **2022**, *17* 064048.
- [17] Z. Hayran, F. Monticone, *Phys. Rev. Appl.* **2024**, *21* 044007.

- [18] J. Yang, J. C. Ke, W. K. Cao, M. Z. Chen, Q. Cheng, V. Galdi, T. J. Cui, *Advanced Optical Materials* **2021**, *9*, 22 2101043.
- [19] M. H. M. Mostafa, M. S. Mirmoosa, S. A. Tretyakov, *Nanophotonics* **2023**, *12*, 14 2881.
- [20] D. Globosits, J. Hüpfel, S. Rotter, *arXiv preprint arXiv:2403.19311* **2024**.
- [21] E. Lustig, O. Segal, S. Saha, E. Bordo, S. N. Chowdhury, Y. Sharabi, A. Fleischer, A. Boltas-seva, O. Cohen, V. M. Shalaev, M. Segev, *Nanophotonics* **2023**, *12*, 12 2221.
- [22] R. Tirole, S. Vezzoli, E. Galiffi, I. Robertson, D. Maurice, B. Tilmann, S. A. Maier, J. B. Pendry, R. Sapienza, *Nature Physics* **2023**, *19*, 7 999.
- [23] H. Moussa, G. Xu, S. Yin, E. Galiffi, Y. Radi, A. Alù, *Nature Physics* **2023**, *19* 863.
- [24] X. Wang, M. S. Mirmoosa, V. S. Asadchy, C. Rockstuhl, S. Fan, S. A. Tretyakov, *Science Advances* **2023**, *9*, 14 eadg7541.
- [25] E. Galiffi, G. Xu, S. Yin, H. Moussa, Y. Ra'di, A. Alù, *Nature Physics* **2023**, *19*, 11 1703.
- [26] J. Sisler, P. Thureja, M. Grajower, R. Sokhoyan, I. Huang, H. Atwater, *Nature Nanotechnology* **2024**, *1*.
- [27] A. Harwood, S. Vezzoli, T. Raziman, C. Hooper, R. Tirole, F. Wu, S. Maier, J. Pendry, S. Horsley, R. Sapienza, *arXiv preprint arXiv:2407.10809* **2024**.
- [28] S. Buddhiraju, A. Dutt, M. Minkov, I. A. D. Williamson, S. Fan, *Nature Communications* **2021**, *12*, 1 2401.
- [29] L. Zhang, Z. R. Huang, X. Q. Chen, Y. N. Zheng, S. Liu, V. Galdi, T. J. Cui, *Advanced Functional Materials* **2024**, *34*, 21 2314110.
- [30] S. Molesky, Z. Lin, A. Y. Piggott, W. Jin, J. Vucković, A. W. Rodriguez, *Nature Photonics* **2018**, *12*, 11 659.
- [31] T. J. Sturges, M. Nyman, S. Kalt, K. Pälssi, P. Hilden, M. Wegener, C. Rockstuhl, A. Shevchenko, *ACS Photonics* **2024**.
- [32] O. Kuster, Y. Augenstein, C. Rockstuhl, T. J. Sturges, *arXiv preprint arXiv:2407.16736* **2024**.
- [33] Y. Zhu, Y. Chen, S. Gorsky, T. Shubitidze, L. Dal Negro, *JOSA B* **2023**, *40*, 7 1857.
- [34] J. Baxter, L. Ramunno, *Opt. Express* **2023**, *31*, 14 22671.
- [35] J. Kim, D. Lee, S. Yu, N. Park, *Nature Physics* **2023**, *19*, 5 726.
- [36] Y. Long, L. Zou, L. Yu, H. Hu, J. Xiong, B. Zhang, *Opt. Mater. Express* **2024**, *14*, 8 2032.
- [37] N. H. Phi, H. N. Bui, S.-Y. Moon, J.-W. Lee, *Advanced Intelligent Systems* **2024**, *6*, 4 2300565.
- [38] M. M. Sadafi, A. F. da Mota, H. Mosallaei, *Applied Physics Letters* **2023**, *123*, 10 101702.
- [39] M. Lobet, N. Kinsey, I. Liberal, H. Caglayan, P. A. Huidobro, E. Galiffi, J. R. Mejía-Salazar, G. Palermo, Z. Jacob, N. Maccaferri, *ACS photonics* **2023**, *10*, 11 3805.
- [40] S. A. R. Horsley, E. Galiffi, Y.-T. Wang, *Phys. Rev. Lett.* **2023**, *130* 203803.

- [41] J. Baxter, A. Pérez-Casanova, L. Cortes-Herrera, A. Calà Lesina, I. De Leon, L. Ramunno, *Advanced Photonics Research* **2023**, *4*, 3 2200280.
- [42] G. Ptitsyn, A. Lamprianidis, T. Karamanos, V. Asadchy, R. Alaei, M. Müller, M. Albooyeh, M. S. Mirmoosa, S. Fan, S. Tretyakov, C. Rockstuhl, *Laser & Photonics Reviews* **2023**, *17*, 3 2100683.
- [43] P. Garg, A. G. Lamprianidis, D. Beutel, T. Karamanos, B. Verfürth, C. Rockstuhl, *Opt. Express* **2022**, *30*, 25 45832.
- [44] P. Waterman, *Proceedings of the IEEE* **1965**, *53*, 8 805.
- [45] P. P. Ewald, *Annalen der Physik* **1921**, *369*, 3 253.
- [46] D. Beutel, I. Fernandez-Corbaton, C. Rockstuhl, *Computer Physics Communications* **2024**, *297* 109076.
- [47] M. Blaber, M. Arnold, M. Ford, *Journal of Physical Chemistry C* **2009**, *113* 3041.
- [48] G. Mie, *Annalen der Physik* **1908**, *330*, 3 377.
- [49] COMSOL, Comsol Multiphysics, <https://www.comsol.com/comsol-multiphysics>.
- [50] JCM, JCM suite: The simulation tool for nano-optics, <https://jcmwave.com/>.
- [51] N. Asadova, K. Achouri, K. Arjas, B. Auguié, R. Aydin, A. Baron, D. Beutel, B. Bodermann, K. Boussaoud, S. Burger, M. Choi, K. M. Czaikowski, A. B. Evlyukhin, A. Fazel-Najafabadi, I. Fernandez-Corbaton, P. Garg, D. Globosits, U. Hohenester, H. Kim, S. Kim, P. Lalanne, E. C. L. Ru, J. Meyer, J. Mun, L. Pattelli, L. Pflug, C. Rockstuhl, J. Rho, S. Rotter, B. Stout, P. Törmä, J. O. Trigo, F. Tristram, N. L. Tsitsas, R. Vallée, K. Vynck, T. Weiss, P. Wiecha, T. Wriedt, V. Yannopapas, M. A. Yurkin, G. P. Zouros, *arXiv preprint arXiv:2408.10727* **2024**.
- [52] N. Stefanou, I. Stefanou, E. Almpanis, N. Papanikolaou, P. Garg, C. Rockstuhl, *J. Opt. Soc. Am. B* **2023**, *40*, 11 2842.
- [53] I. Stefanou, P. A. Pantazopoulos, N. Stefanou, *J. Opt. Soc. Am. B* **2021**, *38*, 2 407.
- [54] E. Panagiotidis, E. Almpanis, N. Papanikolaou, N. Stefanou, *Advanced Optical Materials* **2023**, *11*, 12 2202812.
- [55] J. Bradbury, R. Frostig, P. Hawkins, M. J. Johnson, C. Leary, D. Maclaurin, G. Necula, A. Paszke, J. VanderPlas, S. Wanderman-Milne, Q. Zhang, JAX: composable transformations of Python+NumPy programs, **2018**, URL <http://github.com/google/jax>.
- [56] C. C. Margossian, *WIREs Data Mining and Knowledge Discovery* **2019**, *9*, 4 e1305.
- [57] M. Pelton, *Nature Photonics* **2015**, *9*, 7 427.
- [58] P. E. Stamatopoulou, C. Tserkezis, *OSA Continuum* **2021**, *4*, 3 918.
- [59] E. Stamatopoulou, *Syddansk Universitet. Det Tekniske Fakultet, SDU, Denmark* **2023**.
- [60] V. Giannini, A. I. Fernández-Domínguez, S. C. Heck, S. A. Maier, *Chemical Reviews* **2011**, *111*, 6 3888.
- [61] M. Lyuborav, L. Dikopoltsev, E. Lustig, Y. Sharabi, M. Segev, *Science* **2022**, *377* 425.

- [62] G. Calajò, L. Rizzuto, R. Passante, *Phys. Rev. A* **2017**, *96* 023802.
- [63] J. Park, K. Lee, R.-Y. Zhang, H.-C. Park, J.-W. Ryu, G. Y. Cho, M. Y. Lee, Z. Zhang, N. Park, W. Jeon, J. Shin, C. T. Chan, B. Min, *arXiv preprint arXiv:2404.13287* **2024**.
- [64] R. Yu, S. Fan, *Phys. Rev. Lett.* **2023**, *130* 096902.
- [65] S. Franke, J. Ren, M. Richter, A. Knorr, S. Hughes, *Phys. Rev. Lett.* **2021**, *127* 013602.
- [66] J. Ren, S. Franke, B. VanDrunen, S. Hughes, *Phys. Rev. A* **2024**, *109* 013513.
- [67] R. Citro, M. Aidelsburger, *Nature Reviews Physics* **2023**, *5*, 2 87.
- [68] R. Carminati, J.-J. Greffet, C. Henkel, J. Vigoureux, *Optics Communications* **2006**, *261*, 2 368.
- [69] A. Moroz, *Optics Communications* **2010**, *283*, 10 2277.
- [70] K. Drexhage, *Journal of Luminescence* **1970**, *1-2* 693.
- [71] A. Krasnok, A. Slobozhanyuk, C. Simovski, S. Tretyakov, A. Poddubny, A. Miroshnichenko, Y. Kivshar, P. Belov, *Scientific reports* **2015**, *5* 12956.
- [72] L. Langguth, R. Fleury, A. Alù, A. F. Koenderink, *Phys. Rev. Lett.* **2016**, *116* 224301.
- [73] A. Kwadrin, A. F. Koenderink, *The Journal of Physical Chemistry C* **2012**, *116*, 31 16666.
- [74] A. Rahimzadegan, R. Alaee, C. Rockstuhl, R. W. Boyd, *Opt. Express* **2020**, *28*, 11 16511.
- [75] A. S. Ansari, A. K. Iyer, B. Gholipour, *Nanophotonics* **2023**, *12*, 14 2639.
- [76] S. Tibuleac, R. Magnusson, *J. Opt. Soc. Am. A* **1997**, *14*, 7 1617.
- [77] V. S. Asadchy, M. S. Mirmoosa, A. Díaz-Rubio, S. Fan, S. A. Tretyakov, *Proceedings of the IEEE* **2020**, *108*, 10 1684.
- [78] M. Liu, D. A. Powell, Y. Zarate, I. V. Shadrivov, *Phys. Rev. X* **2018**, *8* 031077.
- [79] Z. Wu, A. Grbic, *IEEE Transactions on Antennas and Propagation* **2020**, *68*, 3 1599.
- [80] H. B. Sedeh, H. M. Dinani, H. Mosallaei, *Nanophotonics* **2022**, *11*, 17 4135.
- [81] D. Ramaccia, D. L. Sounas, A. V. Marini, A. Toscano, F. Bilotti, *IEEE Antennas and Wireless Propagation Letters* **2020**, *19*, 11 1886.
- [82] T. T. Koutserimpas, R. Fleury, *Phys. Rev. Lett.* **2018**, *120* 087401.
- [83] Z. Yu, S. Fan, *Nature Photonics* **2009**, *3*, 2 91.
- [84] A. Rahimzadegan, T. D. Karamanos, R. Alaee, A. G. Lamprianidis, D. Beutel, R. W. Boyd, C. Rockstuhl, *Advanced Optical Materials* **2022**, *10*, 10 2102059.
- [85] H. B. Sedeh, M. M. Salary, H. Mosallaei, *IEEE Access* **2020**, *8* 185919.